The final publication is available at

https://doi.org/10.1016/j.jweia.2022.105065

Additional Information

An automatized methodology to generate velocity distortion panels for wind tunnel testing

A. Broatch[a], X. Margot[a], J. García-Tíscar[a,*], A. Felgueroso[a]

[a]*CMT – Motores Térmicos, Universitat Politècnica de València, Camino de Vera, 46022 Valencia, Spain*

Abstract

Replicating the actual velocity distribution that a target will experience in real life is sometimes necessary to perform realistic aerodynamic characterizations in wind tunnels. In industrial aerodynamics, this is especially critical in aeroengine inlets, automotive and aircraft compressors, atmospheric boundary layers, etc. However, wind tunnels are designed to provide a flow as uniform as possible. To reproduce the desired velocity distribution, the utilization of certain devices for flow adaption is typically required, in a trial-and-error procedure. In this research, we propose a methodology to automatically generate distortion screens to reproduce a desired target velocity distribution, based on analytical relations between the porosity in a media and the total pressure loss induced by this porosity. A numerical routine is used to design a robust and easily-manufactured hexahedral grid that matches the required porosity distribution. Once this geometry is generated, it can be realized by means of widely-available, inexpensive additive manufacturing. To validate the proposed methodology, two geometries that reproduce 1D velocity distributions and another geometry which considers a bi-dimensional distribution have been generated and studied using both computational fluid dynamics and wind tunnel measurements, demonstrating good agreement between the target velocity distributions and those obtained numerically and experimentally.

Keywords: Experimental aerodynamics, Internal flow, Computer fluid dynamics, Flow rigs, Additive manufacturing, 3D printing

1. Introduction

There are many engineering situations in which an environment as controlled as the laboratory is no longer representative for the study of an actual application. For instance, regarding internal aerodynamics, there are few scenarios in which the flow field to be evaluated is as uniform as that of a wind tunnel. Indeed, in general, the variation from the average mean velocity in a wind tunnel test section is within the range of 0.2-0.3% (Barlow et al., 1999) thanks to devices which reduce the turbulence (Kulkarni et al., 2011). However, although in any case the quality of the measurements needs to be controlled and the uncertainties reduced to ensure repeatability (Ocokoljić et al., 2018), a large number of industrial applications present a distorted flow field that has to be implemented in the experiments.

An area where flow distortion plays a key role is the intake of gas turbine engines. The compression system of a gas turbine engine is generally composed of stages of axial compressors. The instabilities that may arise in an axial compressor can be classified into two types (Paduano et al., 2001): surge, which is manifested as an overall oscillation of the annulus-averaged flow in the machine, and rotating stall (Toge and Pradeep, 2017; Lin et al., 2019; Salunkhe et al., 2011), where wavelike disturbances travel circumferentially around the annulus.

Tan et al. (2010) presented a review of different studies that proved the influence of the incoming flow on the compressor performance and the presence of instabilities. However, not only is flow distortion problematic from the point of view of compressor failing, but also as a source of noise emissions (Zenger et al., 2016). The velocity profile has an impact mainly on tonal components, whereas turbulence intensity also influences both tonal and broadband noise.

These days, a tendency towards more integrated systems in aircraft can be seen. Embedded propulsion systems are a clear example of successful integration, but they generate flow distortion at the aerodynamic interface plane. For this reason, a lot of effort is being put into the characterisation of the flow field downstream of a complex intake (Lucas et al., 2014; Tanguy et al., 2018). A closer integration also means a greater interaction with the airframe itself (S-16 Turbine Engine Inlet Flow Distortion Committee, 2017).

Complex embedded intakes and their interaction with the airframe generally lead the propulsion system to suffer boundary layer ingestion (Migliorini et al., 2019; Valencia et al., 2020; Provenza et al., 2019; McLelland et al., 2020)or even vortex ingestion (Frohnapfel et al., 2020; Guimarães et al., 2019). Gorton et al. (2004) developed an active control method which used a 32-port, high mass flow pulsing actuator to reduce the circumferential distortion of an integrated intake measured by the DC60 descriptor (Walsh and Fletcher, 2004) from 29% to 4.6% using less than 1% of inlet mass flow.

Another recent challenge in aeroengines is the need of developing better thermal management systems to dissipate the heat generated in the lubrication circuit of geared turbofans (Hart, 2008). Typically, the use of surface air-cooled oil coolers installed in the bypass duct of the turbofans is sought to

---

Nomenclature

List of symbols

$\dot{m}$	Mass flow rate	kg/s
ϵ	Absolute rugosity	m
γ	Heat capacity ratio	–
A	Area	m^2
c_p	Isobaric specific heat capacity	J/(kg K)
D_h	Hydraulic diameter	m
H	Measurement section height	m
h_{cell}	Height of the cell	m
K	Pressure loss factor	–
L	Screen depth	m
l_{cell}	Length of the cell	m
p	static pressure	Pa
P_0	Total pressure	Pa
Pr	Prandtl number	–
q	Dynamic head	Pa
R	Air gas constant	J/(K mol)
Re	Reynolds number	–
S	Porosity	–
T	Temperature	K
t	Thickness of the cell wall	m
V	Velocity	m/s
y^+	Non-dimensional boundary layer distance	–

List of subscripts

1	Upstream region
2	Downstream region
$cell$	Referred to the cell
f	Referred to the flow

List of acronyms

AM	Additive manufacturing
FDM	Fused Deposition Modeling
PDF	Probability Distribution Function
RANS	Reynolds-Averaged Navier Sotkes
SLA	Stereolithography
SLS	Selective Laser Sintering
TKI	Turbulent Kinetic Intensity

complement existing onboard devices. However, Gelain et al. (2021) demonstrated that the replication of the actual velocity distribution developed inside the turbofan bypass duct plays a key role in accurately characterizing the aerothermal performance of a heat exchanger installed in that location.

Furthermore, during take-off, one of the most restrictive periods in the flight envelope of the aircraft, there are two concerns of great importance. On the one hand, Stojaković and Rasuo (2016a,b) and Stojaković et al. (2018) exposed the problem related to asymmetric flight conditions during low speeds which can endanger the flight performances. The other issue is related to the incoming air to the engine affected by the atmospheric boundary layer. Ameur et al. (2011) studied numerically the impact of this boundary layer on the aerodynamics of the wind-rotor/nacelle interaction. Besides, Saini and Shafei (2021) developed high-fidelity models to predict the flight trajectories of debris, which can be a potential problem in the take-off and landing stages.

The reproduction of these conditions, nevertheless, should not be considered lightly neither numerically nor experimentally. Rasuo (2011, 2012) determined the importance of carefully replicating similarity conditions in terms of Mach and Re number to capture the behaviour of the test models adequately. Moreover, Mirkov et al. (2015) exposed a detailed procedure to numerically simulate complex terrains and capture atmospheric micro-scale flows.

In order to generate a target pressure distribution in wind tunnels or flow rigs to study more accurately the aforementioned situations, the use of distortion panels is widely used. A distortion panel can be seen as a mesh with variable porosity placed perpendicularly to the flow that produces a controlled pressure drop depending on its porosity distribution. From this point of view, it is crucial to be able to determine the re-

lationship between the porosity and the pressure drop. Owen and Zienkiewicz (1957) studied the creation of a uniform shear flow using a grid of parallel rods with varying spacing, observing not only results in close agreement with the theory, but also a non-decaying tendency of the pattern downstream the screen. Phillips et al. (1999) developed a method that used an array of specifically spaced flat plates to reproduce a certain vertical pressure gradient. More recently, Saleem Yusoof et al. (2016) utilised a similar approach based on the wake interaction after radial and circumferential strips of varying widths to modify the flow to test gas turbine engines in ground test facilities, achieving the target Mach profile with a root-mean-square error of 5.06%.

On the other hand, O'Neill (2006) collects a series of different conceptual models that reproduce the distortion panel as a group of punctual aerodynamic sources of a certain strength that interact with the flow and produce the pressure drop. Steiros and Hultmark (2018) extended Koo and James model (Koo and James, 1973), also collected by O'Neil, with the usage of a base-suction term, showing a better fit for low porosities when tested in a water channel.

Later, Schneck et al. (2013) developed a method that divides the incoming flow field into independent streamtubes that suffer a certain drag while passing through the holes in the panel. Using an analytical model, they correlate the drag coefficient of a cell with the pressure drop across that cell.

Huang et al. (2020) manufactured different perforated plates in order to determine the effect of different velocity profiles on a bluff body, by placing the peak velocity at different heights in the tunnel. Hong et al. (2015) modelled the velocity decrease after a windbreake fence by means of genetic algorithms based on their screen porosity, fence height and wind speed. With the aid of additive manufacturing (AM)
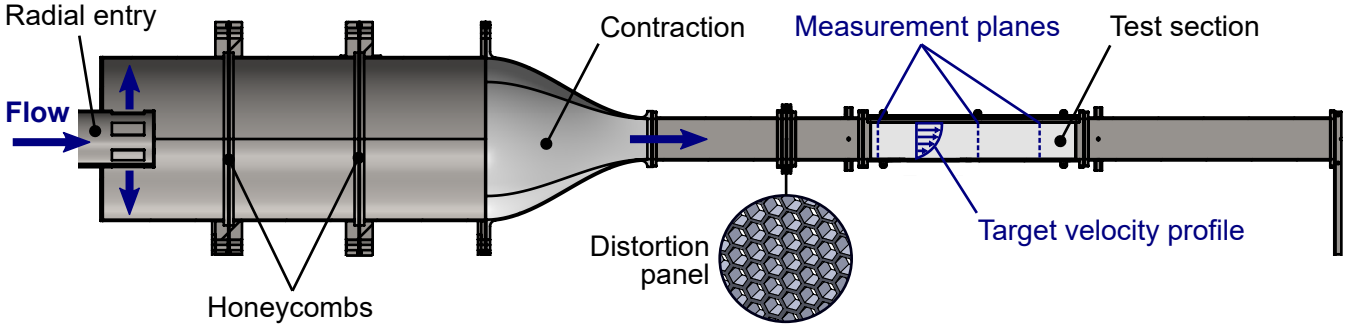
Figure 1: Cutaway of the wind tunnel used in this investigation with the detail of a distortion panel.

and the capabilities of Computational Fluid Dynamics (CFD), Taylor (2019) adapted the empirical model of Roach (1987) to define a conditioning gauze across a turbomachinery annulus to achieve a specific stagnation pressure profile together with a certain flow angle distribution and low turbulence intensity.

Regarding the evolution of the flow field downstream the panel, Stephens et al. (2019) show very little difference at short distances (about one hydraulic diameter) from their distortion panel to replicate boundary layer ingestion in circular ducts. A more detailed study was conducted by Sivapragasam (2019) where the distortion was measured at different locations, numerical and experimentally. Results show how the values of the pressure and its gradients remain almost constant between 2 and 5 diameters, whereas for distances closer than a diameter, the variations were larger.

Additionally to the use of distortion panels, there are other methods (Kozmar, 2021; Catarelli et al., 2020) to generate a boundary layer inside a wind tunnel, or even to simulate twisted wind flows in boundary layers (Tse et al., 2016). Although they are useful for large scale wind tunnels, their application is relegated to the creation of boundary layers, whereas the distortion screes can be used in a more complex manner to modify the flow velocity in the whole section.

In the light of these considerations, it is thus clear that accurate distortion panels are a must for certain kind of wind tunnel tests. Moreover, considering the cost and tight time slots that the use of these facilities entails, a fast procedure that goes from a target pressure distribution to the finished panel in hours rather than days without expensive tryouts is highly desired.

The proposed methodology aims to provide a faster procedure to automatically generate a target velocity distribution. Besides, it is more versatile than other methods which are only capable of reproducing a 1D velocity variation and can be easily used in both, numerical and experimental (see Fig. 1) analysis. Additionally, this methodology is not only inexpensive in terms of manufacturing but also robust and time-saving compared to others based on trial-and-error approaches.

2. Methodology

In order to determine the parameters of the distortion panel, a model based on the study carried out by Overall (1972) has been used. Then, assuming isentropic flow, an algorithm determines the required porosity of the panel, depending on the target downstream velocity distribution which is input by the user. Next, the algorithm computes the geometric parameters required to achieve that porosity for the case of a hexagonal grid, and generates the resulting geometry. Afterwards, this geometry is printed using additive manufacturing. The whole process is thus automatised, allowing rapid testing with many different target velocity profiles.

2.1. Pressure drop model

It is important however to remark certain considerations. The flow is assumed to be uniform with constant velocity and pressure upstream of the panel. Through the panel, it undergoes an isentropic evolution and the static pressure downstream is uniform and constant. As panels are under pressure loads and they may fail during tests (Biswas et al., 2013), a hexagonal grid has been chosen as this type of pattern has good mechanical performance, produces lower pressure drop (Andreassi et al., 2004), tessellates the plane, and is easy to manufacture through AM means. This pattern consists on a base of regular hexagons with the same side used to develop a geometry that modifies the porosity S of each cell by changing the thickness t of the walls and varying the flow area A_f, as can be seen in Fig. 2.

Based on our model and assumptions, four inputs are required to compute the geometry:

1. Static pressure downstream the panel p_2.
2. Height and width of the wind tunnel cross-section H.
3. Number of cells along the vertical length.
4. Maximum porosity S_{max}.

The final objective is to generate a pressure drop along the panel to obtain a certain velocity distribution so, additionally, the target velocity contour v_2 has to be provided. Depending on the number of vertical divisions selected, the algorithm picks the correspondent values of velocity from the contour data.

Knowing the discretized velocity $V_{2_{i,j}}$ and the static pressure, the total pressure and the correspondent mass flow through each cell can be computed through the well-known
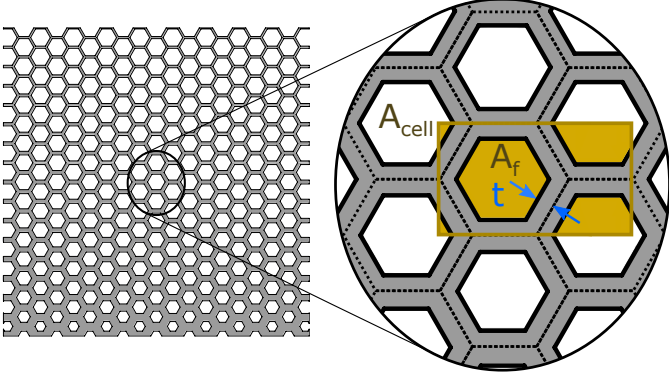
3

Figure 2: Example of hexagonal distortion panel geometry and detail with nomenclature.

isentropic, compressible flow relations:

$$P_{02_{i,j}} = p_2 \left(1 + \frac{\gamma - 1}{2} \frac{V_{2_{i,j}}^2}{\gamma R \left(T - \frac{v_{2_{i,j}}^2}{2C_p} \right)} \right)^{\frac{\gamma}{\gamma - 1}} \quad (1)$$

$$\dot{m}_{i,j} = A_{cell} P_{02_{i,j}} \sqrt{ \frac{2\gamma}{RT(\gamma - 1)} \left[\left(\frac{p_2}{P_{02_{i,j}}} \right)^{\frac{2}{\gamma}} - \left(\frac{p_2}{P_{02_{i,j}}} \right)^{\frac{\gamma+1}{\gamma}} \right] } \quad (2)$$

Here, P_{02} and p_2 are the total and the static pressure downstream the panel respectively, $\dot{m}$ is the mass flow, A_{cell} is the area of the cell (uniform for all the panel), and the subscripts i, j represent each one of the cells in the x and y directions. It is assumed that the static pressure is uniform across the section. The total mass flow will be the sum of that of each cell:

$$\dot{m} = \sum_i \sum_j \dot{m}_{i,j} \quad (3)$$

The rest of the parameters have to be calculated iteratively. The first step is to guess an average porosity of the panel. Ecker et al. (1976) proposed a method to estimate the total pressure loss K through thin honeycomb systems. Thus,

$$K = 0.214 \left(\frac{\epsilon}{D_h} \right)^{0.4} \left(3 + \frac{L}{D_h} \right) \frac{1}{\bar{S}^2} + \left(\frac{1 - \bar{S}}{\bar{S}} \right)^2 \quad (4)$$

where ϵ is the absolute rugosity of the panel walls, D_h is the hydraulic diameter of the hexagonal cells, L is the thickness of the panel in the flow direction and $\bar{S}$ is the average porosity.

Now, with the maximum porosity, the total pressure upstream of the panel can be computed. The selection of the maximum porosity is a critical step: higher porosity and thus higher free area will reduce pressure loss, but will also result in a thinner mesh with lower structural integrity. Furthermore, as the objective is to manufacture the panel through AM, the maximum resolution of the printer also plays a key role in the decision of the maximum porosity. The maximum flow area and the porosity are related by:

$$A_{f,max} = A_{cell} S_{max} \quad (5)$$

The total pressure at the panel section is considered to be uniform. A first guess of the static pressure is needed to begin an iterative process to calculate the conditions of the flow upstream the panel. With the static pressure, the total pressure upstream the panel can be obtained as:

$$\dot{m}_{max} = A_{f,max} p_1 \frac{ \sqrt{ \frac{2}{RT} \frac{\gamma}{\gamma-1} \left[1 - \left(\frac{p_1}{P_{01}} \right)^{\frac{\gamma-1}{\gamma}} \right] } }{ \left(\frac{p_1}{P_{01}} \right)^{\frac{\gamma-1}{\gamma}} } \quad (6)$$

On the other hand, the velocity before the panel can be derived from the isentropic equations for compressible flow:

$$\frac{P_{01}}{p_1} = \left[1 + \frac{\gamma - 1}{2} \frac{v_1^2}{\gamma R \left(T - \frac{v_1^2}{2C_p} \right)} \right]^{\frac{\gamma}{\gamma-1}} \quad (7)$$

Once the flow field is modelled, the loss factor through the panel is defined as:

$$K' = \frac{P_{01} - \bar{P}_{02}}{q_1} \quad (8)$$

As the total pressure after the panel is not uniform, an average $\bar{P}_{02}$ is considered. This value K' is compared against the one obtained previously. Until a certain convergence criteria is reached, the value of the static pressure is therefore modified by:

$$p_1 = \frac{ \bar{P}_{02} }{ \left[1 + \frac{\gamma-1}{2} \frac{v_1^2}{\gamma R \left(T - \frac{v_1^2}{2C_p} \right)} \right]^{\frac{\gamma}{\gamma-1}} - \frac{K v_1^2}{2R \left(T - \frac{v_1^2}{2C_p} \right)} } \quad (9)$$

Once convergence has been reached, the porosity of each cell can be computed straightforward:

$$S_{i,j} = \frac{ \frac{\dot{m}_{i,j} \sqrt{T}}{A_{cell} P_{01}} }{ \sqrt{ \frac{2\gamma}{RT(\gamma-1)} \left[\left(\frac{p_2}{P_{02_{i,j}}} \right)^{\frac{2}{\gamma}} - \left(\frac{p_2}{P_{02_{i,j}}} \right)^{\frac{\gamma+1}{\gamma}} \right] } } \quad (10)$$
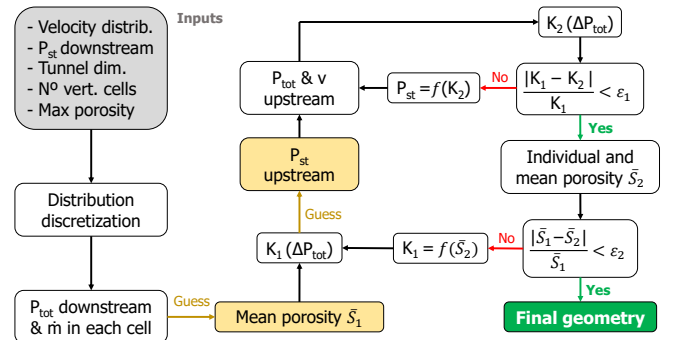

Figure 3: Flow diagram of the process to determine the porosity.
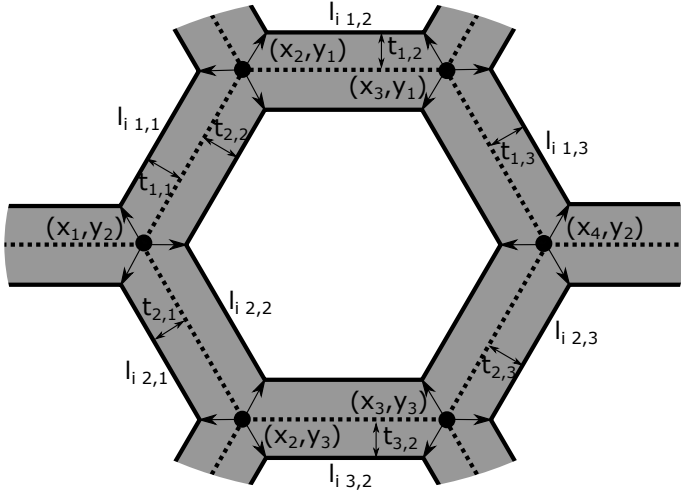
Figure 4: Sketch of the base grid distribution and the final vertices location depending on the thickness of each cell.

Finally, the average of the porosity is calculated. If the comparison between the value obtained and the first guess to derive the loss factor does not satisfy a convergence criterion, the whole process is restarted with the new averaged porosity. If the criterion is met, then the algorithm generates the geometry. This process is summarised in Fig. 3.

2.2. Geometry generation

Once a porosity distribution $S_{i,j}$ has been selected, the proposed algorithm will generate a variable hexagonal grid that reproduces this distribution. To this end, a base geometry made of regular hexagons is used to begin the process. The side of these hexagons depends on the number of discretized elements along one side of the section and the length of the side.

A series of points from the base hexagons' vertices can be now uniformly distributed throughout the surface. It is important to notice that, for this particular distribution, the coordinates of the vertices follow a repetitive pattern in which the horizontal and vertical points of the grid can be obtained from

$$x_i = x_{i-1} + l_{cell} \frac{1-(-1)^i + \cos 60° \left[1+(-1)^i\right]}{2} \quad (11)$$

$$y_j = y_{j-1} + \frac{h_{cell}}{2} \quad (12)$$

where l_{cell} and h_{cell} are the horizontal length and height of the cell. All the x_i coordinates are equal in every row and the same with the y_j in each column. It has been considered that $x_1 = y_1 = 0$

Now there is a grid of points from the base geometry and, since the porosity distribution can be expressed as a function of the side of the base hexagon and the thickness of each cell $t_{i,j}$, the interior side of the hexagons (which will be the side of the holes to be manufactured) can thus be computed. A sketch that depicts the step from the base size geometry to

the final locations of the vertices from the interior side of the hexagons depending on the thickness of each cell is displayed in Fig. 4.

Finally, with these values calculated, each hexagon is drawn storing the values from its vertices in columns, i.e. two matrices with x and y coordinates and as many columns as the total number of hexagons. The matrices are exported as a DXF file, which can be read by most CAD software, There, they are imported as a series of curves in a plane. Then, these curves are used to extrude and cut the 3D panel to the shape required at the wind tunnel, in addition to fitting any required anchoring system particular to the tunnel.

It is important to notice two points. On the one hand, the repetitive cell is adjusted to one of the sides of the section, in Fig. 2 this is the vertical side, so the porosity along the vertical direction is well defined for all the cells, whereas for the horizontal discretization, the porosity in the boundaries may not be the expected one. However, these events are assumed to be negligible. Additionally, once the total length of the cells is calculated, they are all shifted so the final geometry is centered in the section. On the other hand, the hexagons can be divided into two groups: columns with full hexagons in the cell and columns that include partial hexagons in the cell. To generate regular hexagons, the ones from the columns that are partially included in several cells, have the averaged thickness of the 4 cells in which they are included. This assumption is valid as long as the contours of the velocity are smooth.

2.3. Manufacturing

A crucial step of the proposed methodology is the rapid and automated manufacturing of the generated geometry. With the advent of additive manufacturing (Gibson et al., 2014), several mature and widely available technologies exist to fulfil this step.

The most extended AM principle is typically known as Fused Deposition Modeling (FDM), where a thermoplastic
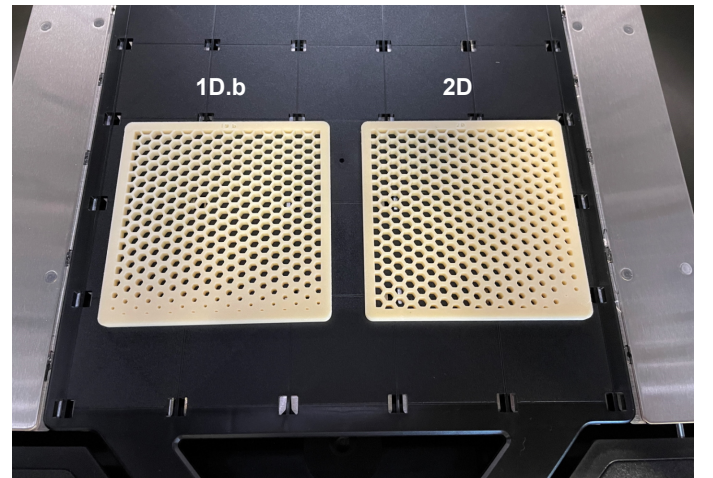

Figure 5: Two distortion screens 3D-printed in ABS through the FDM technique. These correspond to geometries 1D.b and 2D described in subsection 2.4.

filament is fused and deposited, layer after layer, through an extruder head whose position is controlled by a computer. Professional-grade 3D printers based on this principle are relatively affordable, and as such, they are available at many research laboratories and workshops.

Other popular AM techniques include Selective Laser Sintering (SLS) and Stereolithography (SLA), although professional or industrial-grade machines of these types are still less readily available at workshops. In this investigation, a Stratasys F170 professional-grade FDM printer was used to print the geometry in ABSplus thermoplastic. This machine is capable of a minimum layer height of 0.13 mm, and this is as well the minimum wall thickness, which must be taken into account when designing the panel. In Fig. 5 two sample

distortion panels are shown after the printing process is complete. Note that in order to use ABS-type materials, use of support material and confined, temperature-controlled build chambers are recommended in order to avoid warping.

A trade-off between pressure loss and mechanical performance must be reached considering the properties of the AM material, the printing resolution, and the AM principle. In this regard, when using an anisotropic method such as FDM, care should be put to ensure that the mechanical stresses are aligned with the XY axes of the printed panel in order to prevent delamination and to ensure optimum load bearing. Heat deflection and chemical resistance must also be considered, especially in closed wind tunnels with smoke-based streamline visualization or seeding for laser instrumentation.
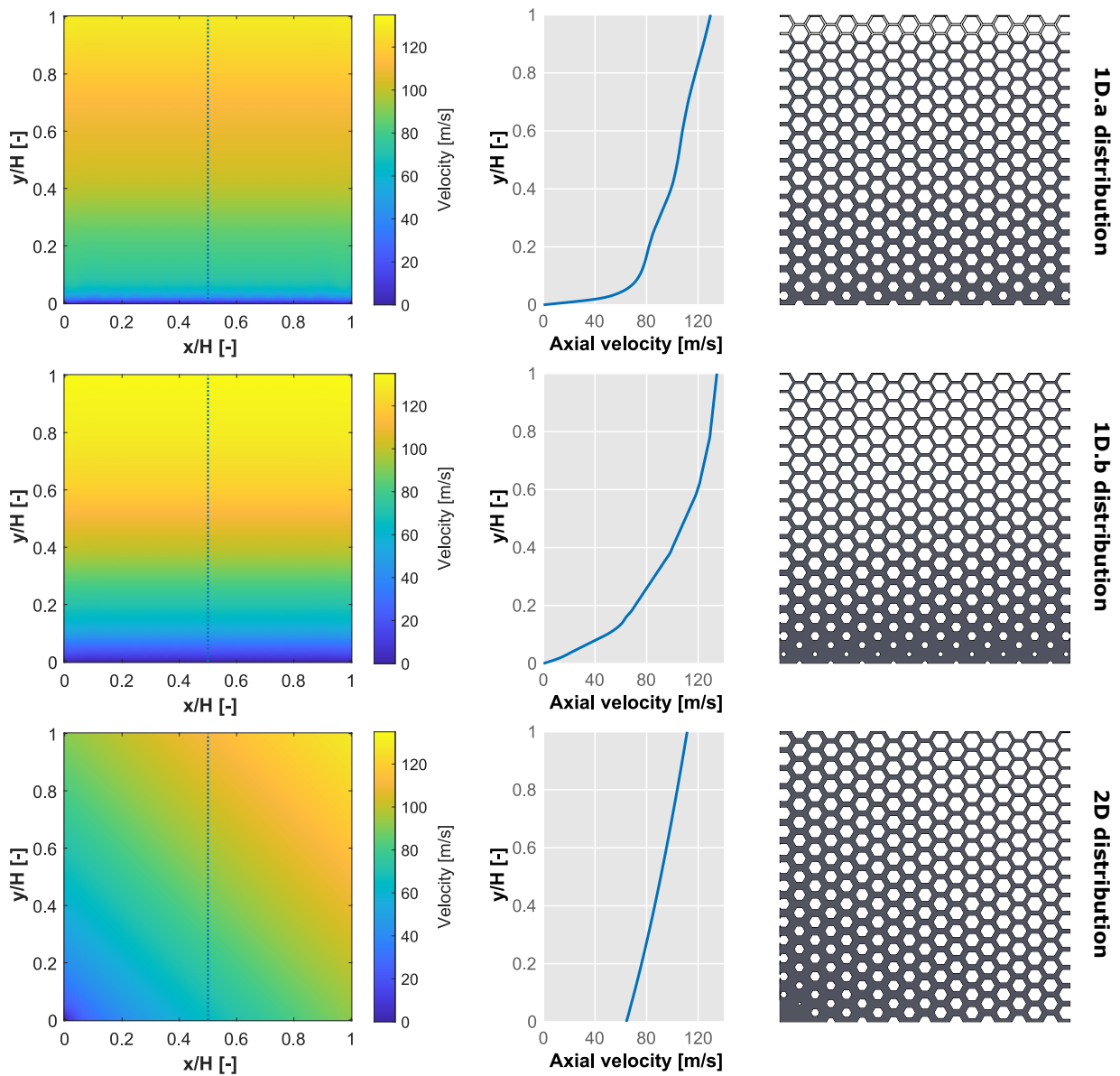

Figure 6: On the left, velocity distributions targeted in the cases 1D.a, 1D.b and 2D. Centered, magnitude of the axial velocity along the vertical center line (displayed as dotted line in the contours). On the right, the outcome geometry from the analytical process to generate each velocity distribution.

In these cases, it may be preferable to realize the screens through subtractive techniques such as CNC machining or laser cutting. The latter is especially well suited for the proposed routine since the resulting DXF files can typically be sent directly to manufacturing services. However, in most cases, AM provides good results with fast turnaround times and extremely affordable costs.

2.4. Velocity distribution targets

Three different velocity distributions are going to be considered. The former two consist of 1D velocity variations that simulate different boundary layers and the latter is a 2D velocity distribution. The cases are: 1D.a, which is a relatively smooth boundary layer still in development; 1D.b, a more severe boundary layer that is already developed in the uppermost region; and 2D, a distribution consisting of a diagonal velocity gradient from one corner to the opposite one. The target velocity distributions and the shape of the velocity profiles along the center line are displayed in Fig. 6. The actual FDM-manufactured screens corresponding to the 1D.b and 2D targets were shown in Fig. 5. Note that these are idealized velocity distribution targets in the sense that, for instance, no provision is made for a boundary layer along the top and lateral walls.

3. Numerical analysis

In order to better understand the behaviour of the flow downstream of the proposed distortion screens, and to determine the accuracy of the analytical design method, a numerical analysis is conducted by means of CFD. The same numerical setup will be used to consider the three different aforementioned targets of velocity distribution.

3.1. CFD setup

The simulation is carried out using the STAR-CCM+ CFD solver which uses a finite volume method. The equations governing the flow characteristics are conservation of mass, momentum and energy. Assuming also the air to be an ideal
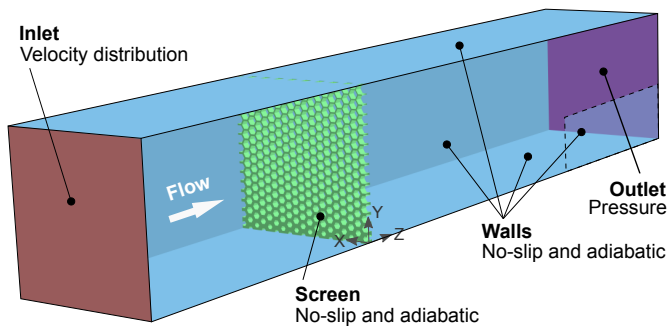

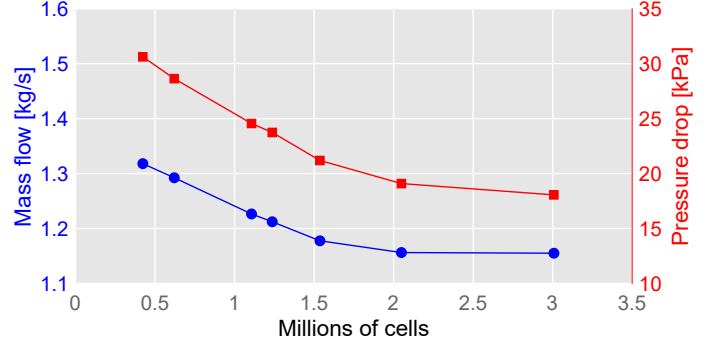**Figure 7:** Schematic of the computational domain with its boundary conditions.

Figure 8: Mesh convergence study comparing values of mass flow (blue points, left axis) and pressure drop (red squares, right axis) as function of the number of cells.

compressible gas under steady-state and turbulent conditions, the final non-dimensional equations to be solved are:

$$\frac{\partial \rho u_i}{\partial x_i} = 0, \tag{13}$$

$$\frac{\partial \rho u_i u_j}{\partial x_j} = -\frac{\partial p}{\partial x_i} + \frac{\partial}{\partial x_j}\left[\frac{1}{Re}\left(\frac{\partial u_i}{\partial x_j} + \frac{\partial u_j}{\partial x_i}\right) - \rho \overline{u_i' u_j'}\right], \tag{14}$$

$$\frac{\partial \rho u_i T}{\partial x_i} = \frac{\partial}{\partial x_i}\left(\frac{1}{RePr}\frac{\partial T}{\partial x_i} - \rho \overline{u_i' T}\right) \tag{15}$$

where Re and Pr are the Reynolds and the Prandtl number, defined as $Re = v_1 H/v$ and $Pr = C_p \mu/k_f$, being H, v, C_p, μ and k_f the height of the tunnel, the kinematic viscosity, the specific heat coefficient, the dynamic viscosity and the conductivity, respectively.

A Reynolds-Averaged Navier Stokes (RANS) approach is used to model the turbulence in the control volume. Particularly, a $k-\omega\ SST$ (Menter, 1993) with a Gamma turbulent transition scheme is selected to this purpose. The turbulence model has been selected since it uses a pure $k-\omega$ approach in the inner boundary layer, not needing any damping function close to the walls and being considered a Low-Re turbulence model. Additionally, as the flow gets further from the walls, the model transitions towards a $k-\epsilon$ model to get rid of the typical sensitivity of $k-\omega$ models to the freestream turbulence properties. Besides, by assuming that the main shear-stress is proportional to the turbulent kinetic energy, the model predicts a better behaviour when the boundary layer is subjected to adverse pressure gradients. The Gamma transition model simplifies the GammaReTheta transition model, which uses two equations, one for the intermittency and another one for the transition momentum thickness Reynolds number, but some coefficients need to be specifically calibrated in a large time-consuming process, so the simplified model avoids the Re_θ equation and is calibrated against a considerable number of Falkner-Skan flows under several test conditions (Menter et al., 2015). A coupled flow solver with an implicit second order upwind discretization scheme has been used.

The control volume is a square duct that begins 2 hydraulic diameters upstream of the screen and continues for 4 extra diameters downstream it. With this, the incoming flow can
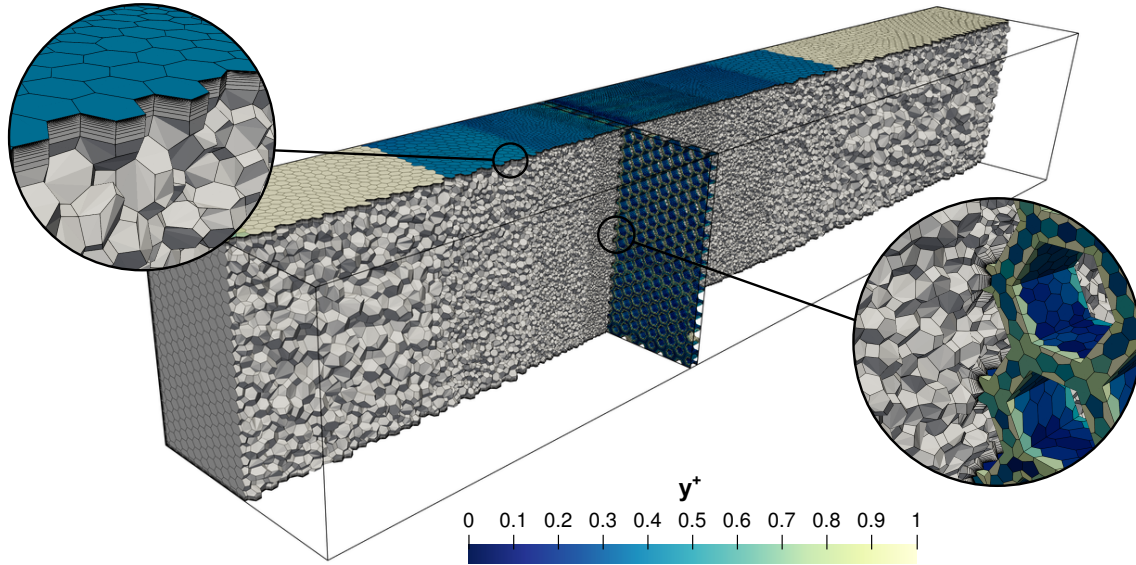
Figure 9: Final 2-million-cell mesh with mesh details close to the tunnel walls and around the distortion screen, colored by y^+.

develop before reaching the screen and the impact of the panel can be considered upstream too. Besides, the length downstream of the gauze enables to determine the duration of the influence in the distorted flow.

Boundary conditions were selected to match the experimental conditions that will be used to validate the simulation. In the inlet, the velocity distribution measured without the distortion screen is imposed and the static pressure chosen for the outlet condition is one typically found during the experiments. The case is assumed to be adiabatic since no heating sources appear in the problem and the temperature at both inlet and outlet is set to 300 K. In all the walls of the domain, those from the tunnel and the correspondent to the distortion screen, no-slip conditions are also imposed. A schematic of the domain used during the simulations together with the boundary conditions imposed can be seen in Fig. 7.

As is customary with CFD setups, the first step is to perform an independence mesh study. To do so, the 1D.a case is used and the parameters and characteristics of the mesh developed and considered independent are used in the other two cases. Figure 8 represents the values of the mass flow and the pressure drop between domain inlet and outlet depending on the millions of cells used. It is noticeable how the pressure drop is practically the same in the cases of 2 and 3 million cells. Besides, regarding the mass flow, the values obtained in that cases are almost constant.

For these reasons, the final mesh configuration is composed of a little more than 2 million cells. Furthermore, three different volumetric control regions refine the mesh size in the surroundings of the screen. This final mesh is mainly composed of polyhedral unstructured cells, although close to the walls there is a transition towards prismatic cells parallel to them in order to better solve the boundary layer.

To this end, the size of the cells also decreases in order to

obtain values of $y^+ \leq 1$ on all the walls and especially on the screen, with the objective of properly resolving the viscous sublayer, which has a crucial effect on the working of the distortion panel, especially for the smaller openings. Besides, with the three different volumes used to refine the size of the cells close to the panel, values in the order of the 25% the base size can be reached. These volumes are imposed so the transition until the thinner mesh is carried out smoothly and to obtain a better spatial resolution, mainly in the wake after the screen, but also in the upstream region, since close to the screen the flow field is also slightly perturbed. Fig. 9 shows the final mesh layout with details in the walls and the surroundings of the distortion screen.

3.2. CFD results and discussion

In the first place, results will be analysed along the center line and compared against the targets. To do so, the turbulent and mixing region after the screen needs to settle and reach uniform conditions. Typically, after two hydraulic diameters the flow has recovered a stable situation, so the results will be presented in that region.

Figure 10 displays the velocity contours for the different cases, together with their deviation when comparing the CFD results with the target. It must be remarked that all profiles present high deviations compared to the target in the uppermost and lowermost regions.

This occurs because the top of the profiles, as they are theoretical, do not consider that velocity goes to zero close to the walls, forming necessarily a boundary layer with low velocities. The bottom of the section is influenced by the impact of low velocities in the calculation, i.e. a small deviation from a small target leads to a high percentage. Besides, the theoretical target for the 2D case does not consider either that velocity will be zero at the wall.
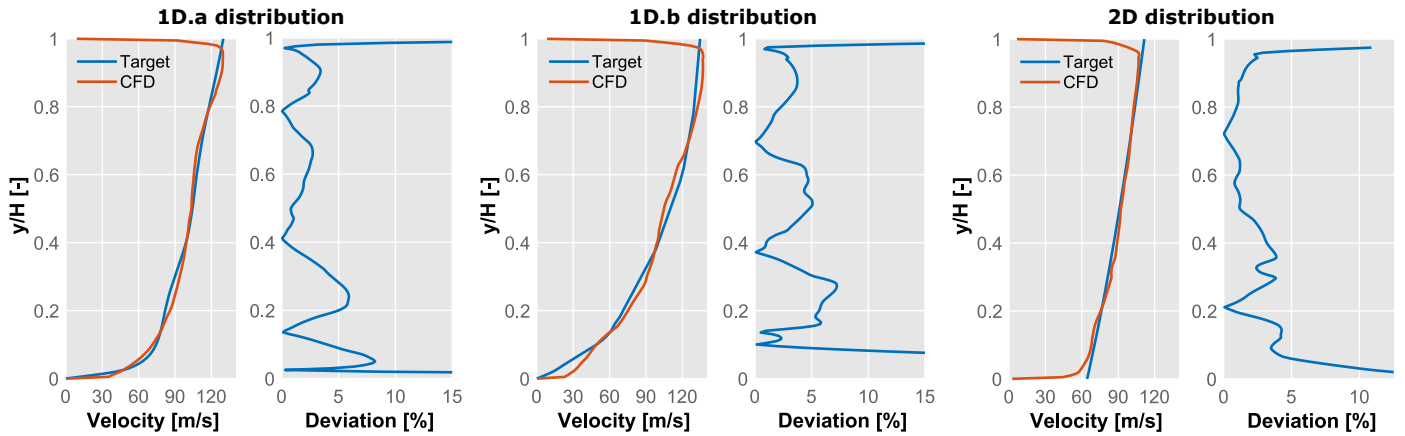
Figure 10: Comparison between the three different target velocity profiles in the center of the section and the CFD results along the vertical center line 2 hydraulic diameters downstream the distortion screen with the deviation from the target in each case.

The 1D.a case presents a very good match for the whole channel height, oscillating only slightly around the target values. In any case, as the deviation graph shows, the discrepancies between both profiles are typically below 3%, except for a couple of regions close to the bottom where it increases up to 7%. Regarding the 1D.b case, the fluctuations in the results obtained with CFD are higher than in the first case, although also following the trend of its target. This can also be seen in the higher values of deviation, that reaches values of 5%. Furthermore, the bottom-most region is not perfectly captured, presenting higher values in the simulation, which induces larger deviation values at higher values from the bottom. Finally, the profile in the 2D case is reproduced with high accuracy during practically all the height, being relatively stable. This is translated into very low deviations, always below 5%, disregarding of course the top and bottom of the region, where the CFD considers the presence of a boundary layer that the theoretical target obviates.

Other important results are the velocity contours in the downstream region of the screen. It is obvious for the 2D case in which not only the reproduction of the velocity profile could be important, but the capability of the method to recreate a bi-dimensional velocity distribution. However, it is also interesting to see how the velocity profiles in the one-dimensional cases behave in the whole section.

With this purpose, Fig. 11 represents, in the first two columns, the values of the target velocity distribution and that obtained numerically, and in the last column, the deviation values between them. It must be mentioned that the deviation values are capped at 10% in order to be able to see the distribution in the larger part of the section. It is important to note that the incoming flow distribution has a rather important influence on the way the screen behaves and thus, its performance. This is because the analytical model assumes an idealized, constant inlet velocity distribution whereas the CFD model considers the actual velocity measured in the experimental wind tunnel.

The first velocity distribution, 1D.a case, is very similar to the target one and the values seem quite uniform along the horizontal direction, although it is possible to see that the changes in velocity occur in a blurrier transition instead of uniformly as in the target. The deviation in this case is also quite uniform horizontally with values typically below 4%, presenting the maximum values close to the bottom and surrounding the walls due to the boundary layer.

In the 1D.b case, the results are very alike. The numerical results are very similar to the target, with faster velocities in the bottom as happened in Fig. 10, and present relatively good horizontal uniformity. Here, the deviation is a bit larger, but with values under 6% in general except for the lower zone and close to the walls, where they increase.

It is, in any case, the 2D distortion screen the one that presents a higher interest in this representation. The velocity computed displays a bi-dimensional distribution very similar to the target. It can be clearly seen the diagonal pattern induced by the distortion screen is replicating with high accuracy the desired distribution. Indeed, looking at the deviation contour, the values are typically around 3-4%, disregarding a region in the bottom left of the section where lower target velocities are desired. Note that the velocity distribution has limitations regarding spatial changes in velocity and could not work adequately if they are too abrupt or if, as in this case, there are regions with velocities close to zero in one corner and close to 130 m/s in the opposite one.

One last thing which must be remarked about Fig. 11 is the distribution of regions with the same or very similar values of deviation. The one-dimensional cases present these iso-deviation values mainly following horizontal patterns, whereas in the 2D case are distributed basically in diagonals.

Once the velocity distribution has been achieved, it is also important to determine the duration of this disturbance. In Fig. 12, the evolution of the velocity profile generated by the distortion screen 1D.a along the center line at several hydraulic diameters (D_H) is displayed. It is shown that in the closest distances (left plot) there is a tendency to replicate the final velocity profile, but the perturbations induced by the screen and the mixing region are still very present.
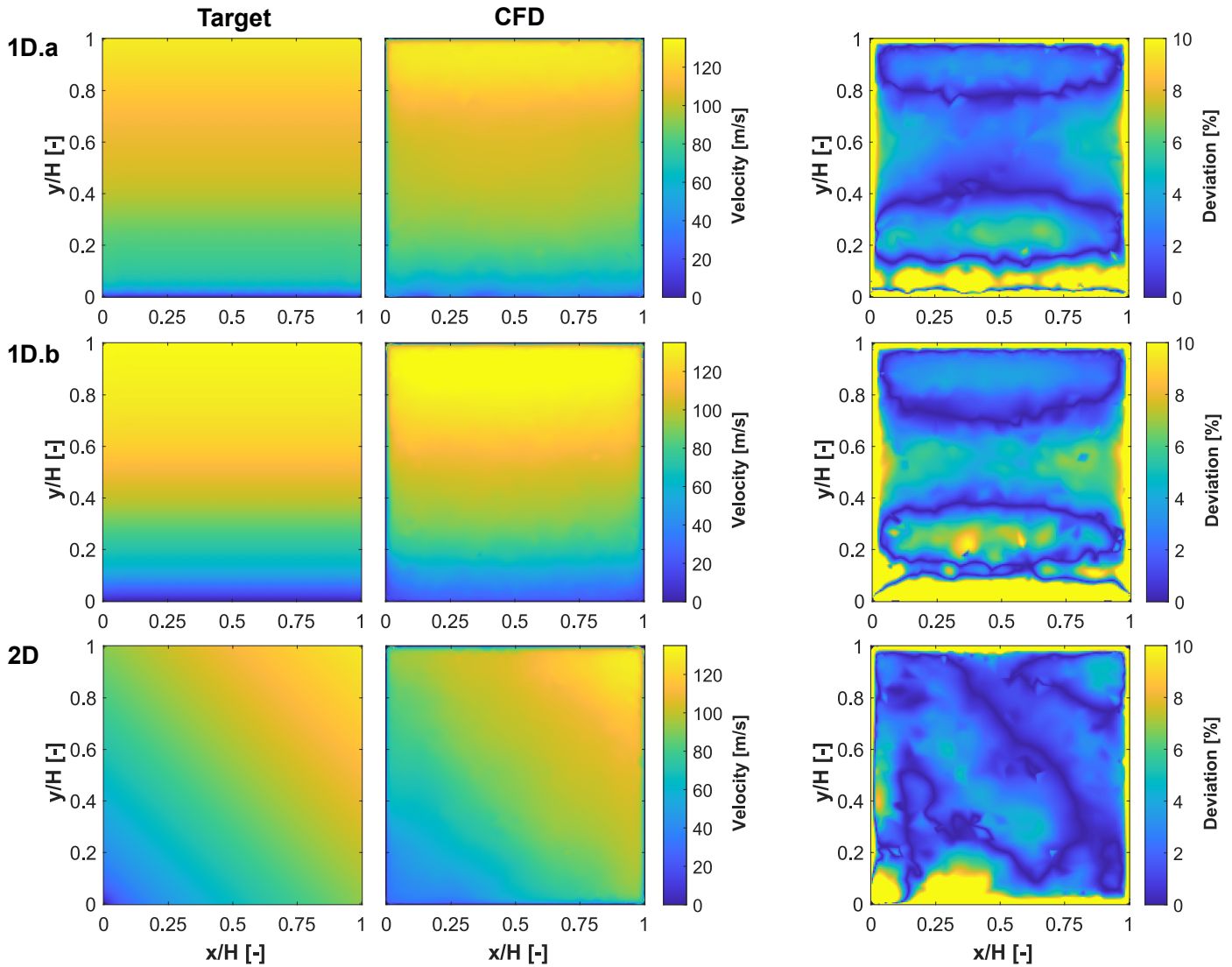
Figure 11: Comparison of the target velocity contours and the results obtained in CFD two hydraulic diameters downstream the distortion screen with the deviation between them.
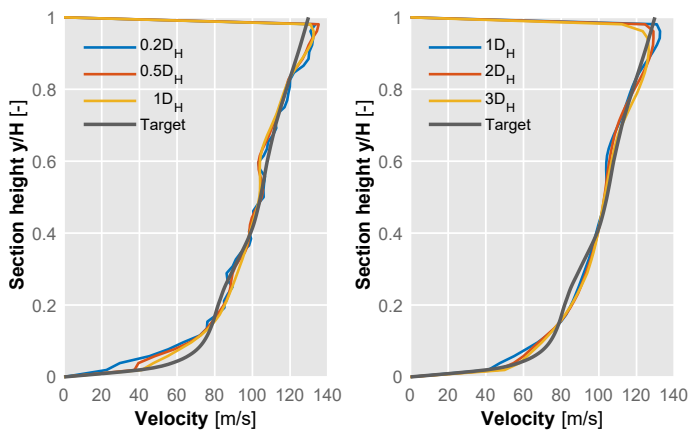

Figure 12: Evolution of the velocity profile at different hydraulic diameters downstream the distortion screen.

Further diameters downstream (right plot), nevertheless, the outcome is much smoother and one hydraulic diameter downstream the final distribution is almost achieved. On the other hand, the distorted velocity appears to be stable after 2 hydraulic diameters and maintains the shape downstream.

Apart from the velocity field modification based on different pressure drops, the fact that the distortion screen interacts with the fluid produces turbulence. Fig. 13 displays the evolution of the turbulent kinetic intensity (TKI) in the domain for each case. It can be seen how the incoming flow presents a relatively low and uniform field but downstream the gauze values increase in the region where the porosity is lower (smaller orifices).

As a matter of fact, the larger values can be distinguished in the 1D.b case, where there is a large region with low porosity, but also the 2D case presents large values downstream of the region where the speed drops substantially. Nevertheless, as the flow travels further downstream the distortion
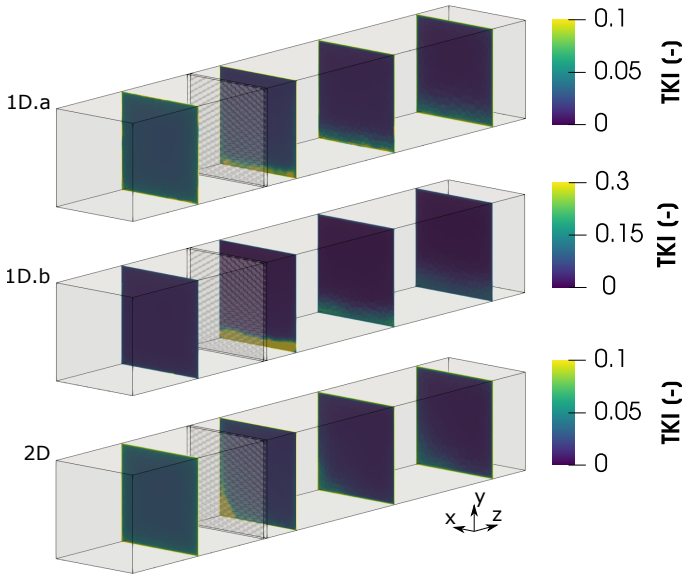
Figure 13: Evolution of the turbulent kinetic intensity (TKI) across the numerical domain.
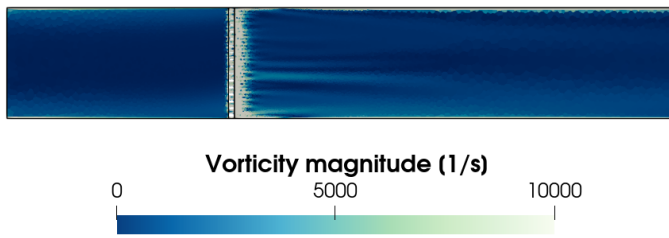

Figure 14: Evolution of the vorticity in a longitudinal plane across the numerical domain.

panel, the turbulent peaks decay to values relatively uniform across the section. Besides, it can be seen how the turbulence after the panel is reduced in the zones with larger holes compared to the upstream values, which implies a behaviour of the screen similar to that of a honeycomb straightener, as long as the porosity is large enough. This is a byproduct of the velocity distortion process that could be advantageous in some applications.

This however highlights the importance of allowing for enough downstream space for the flow to develop adequately after the distortion screen. By plotting the vorticity magnitude in Fig. 14, it can also be seen that just downstream the screen the vorticity increases with regards to the initial freestream conditions, but by the time the flow reaches the outlet of the domain, these vortical structures have subsided and the flow has returned to vorticity conditions similar to the inlet.

4. Experimental validation

Although CFD results may provide an accurate insight into the behaviour of the flow, it is crucial to validate them against experimental tests, since major assumptions and models are used when building a simulation. For this purpose, the three proposed geometries were manufactured and installed in a wind tunnel. The velocity distribution measured in this facility when the distortion screens are not installed is the one used as the inlet boundary condition for the numerical simulations.

4.1. Wind tunnel setup

The facility utilized to perform the experimental tests is composed of a flow rig that supplies a wind tunnel. A two-stage centrifugal 500 kW electrical compressor is responsible to deliver up to 2.15 kg/s of mass flow at 3 bar(A). A series of valves can chock and bleed out the flow to provide the desired pressure and mass flow to the test chamber. Two settling tanks of 3 m^3 are distributed along the line to protect the compressor in particular and the facility in general from sudden changes in the operating condition.

The wind tunnel (already shown in Fig. 1) begins with a small settling chamber to stagnate the fluid before it arrives to the test section. The entry to the settling chamber is a pierced pipe engineered following Purdue's PETAL facility design (Paniagua et al., 2018). To eliminate turbulent structures in the chamber, two honeycombs straighteners are used to laminate the flow. Then, a smooth transition guides the air from the circular settling chamber to a square duct with sufficient length for the flow to develop a uniform velocity distribution, until it reaches the distortion screen which is mounted in a dedicated flange.

Downstream the distortion panel, a straight duct lets the new flow structure to accommodate to its new distribution before entering the test section of the tunnel. Since the main idea of the distortion screen is to generate a particular velocity distribution to analyse this impact on components in the test section, the measurement location is shortly after the beginning of this region. The screen is far enough, 2.3 hydraulic diameters, for the flow to reach stationary conditions. Then, the air goes through the test section and is expelled facing an extractor with a silencer. A more detailed explanation of the facility was provided by Chavez Modena et al. (2021).
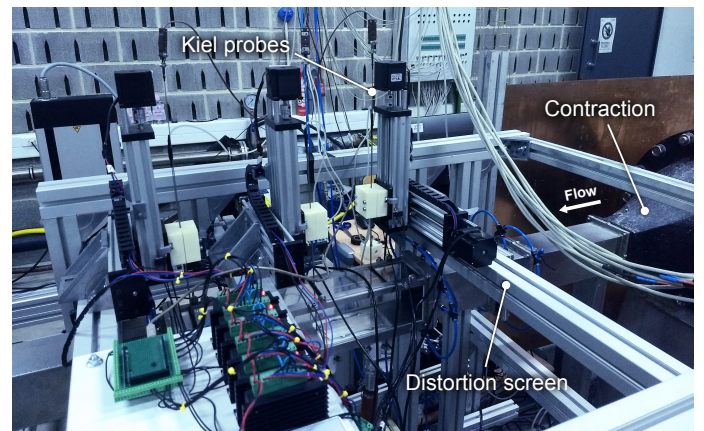

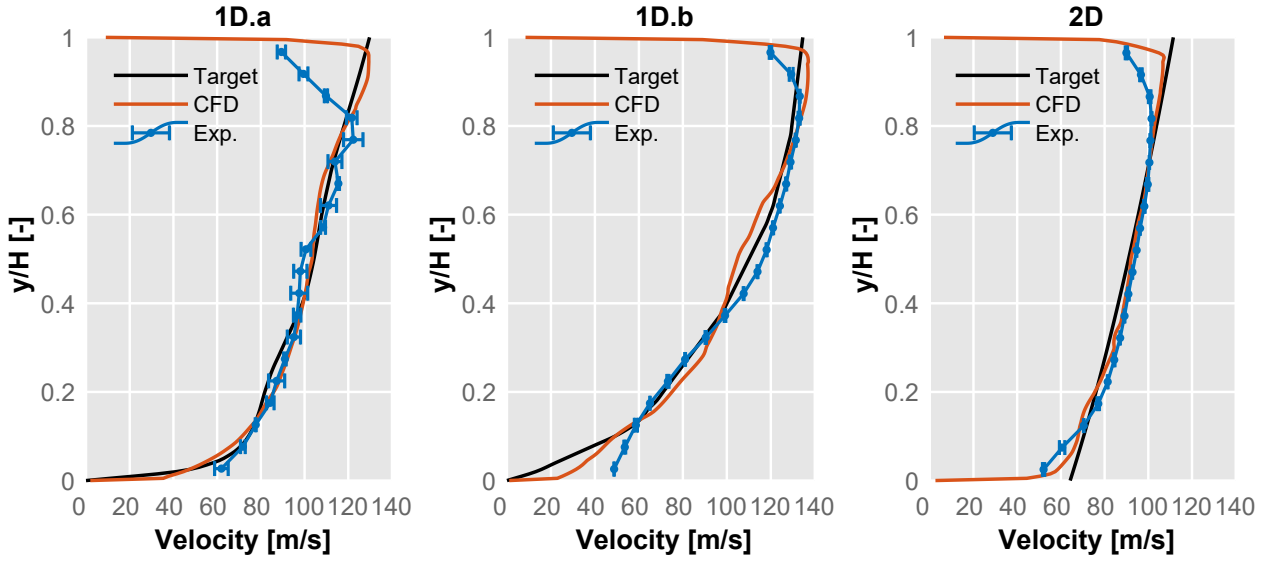**Figure 15:** Image of the wind tunnel in which the experimental validation was carried out.

Figure 16: Experimental validation of the velocity profiles, comparing the values from the experiments, the numerical simulation and the target for each case. Error bars in the experimental data show the standard deviation for different measurement runs (two for each panel).
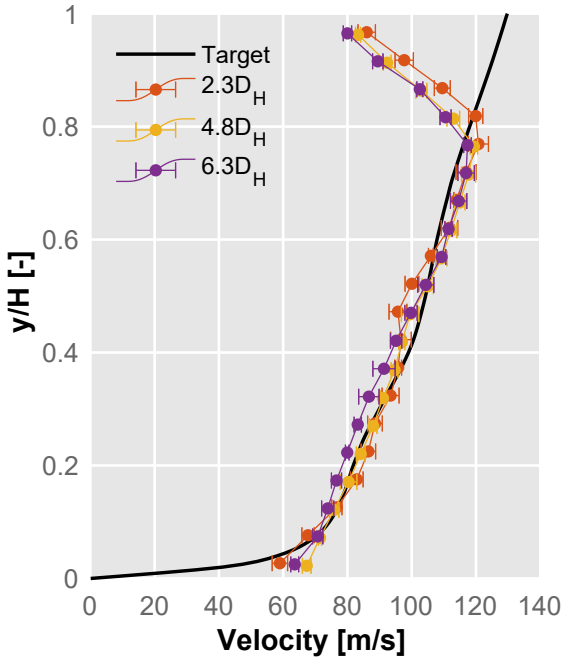

Figure 17: Evolution of the velocity profile for the 1D.a case at different hydraulic diameters D_H downstream the panel. Error bars show standard deviation.

Aerodynamic measurements are performed by means of a Kiel probe, a type of probe with a shielded head that measures total pressure and is not influenced by turbulence or flow misalignment; it is introduced in the tunnel through an opening in the upper wall featuring felt strips and positioned with a bi-axial traverse system. For the static pressure, a piezometric ring that connects 8 static pressure ports, 2 per wall, to derive the mean value in the section is used. Both pressure measure-

ments are not co-planar, but being 0.65 hydraulic diameters upstream in a straight pipe, the static pressure is assumed to be practically the same. The pressure ports are connected to GE UNIK 5000 piezoresistive sensors which are read by a NI-PXI DAQ system. All controls, DAQ and traverse, are centralized in a computer running a MATLAB measurement routine. The experimental setup can be seen in Fig. 15.

4.2. Experimental results

Using this setup, all three distortion screens were tested at each nominal flow condition (3650 kg/h, 3360 kg/h and 2760 kg/h respectively) and 300 K, with the backpressure being slightly higher than the ambient. The most upstream Kiel probe, highlighted in Fig. 15, was used to characterize the cross-section of the tunnel at 2.3 hydraulic diameters from the distortion screen. This probe was also used to obtain the velocity information without the distortion screen that was imposed as inlet boundary condition in the CFD setup.

In Fig. 16, the comparison of the three experimental results in the center line are compared against the CFD prediction. As it can be seen in the figure, the final velocity distribution of the profile 1D.a is almost identical to both numerical prediction and target for most of the height. The upper part presents a certain discrepancy with the prediction, maybe caused by some interactions between the upper boundary layer and the distortion screen. On the other hand, the results shown in the case 1D.b are the opposite: although in general there is a good match between the three profiles, the lower region measured in the tunnel presents an excess of velocity compared with the target. This behaviour seems to be partially captured by the CFD, since it depicts an increase in velocity with a similar slope to that of the experiments in that zone. In the last case, nevertheless, the velocity profile
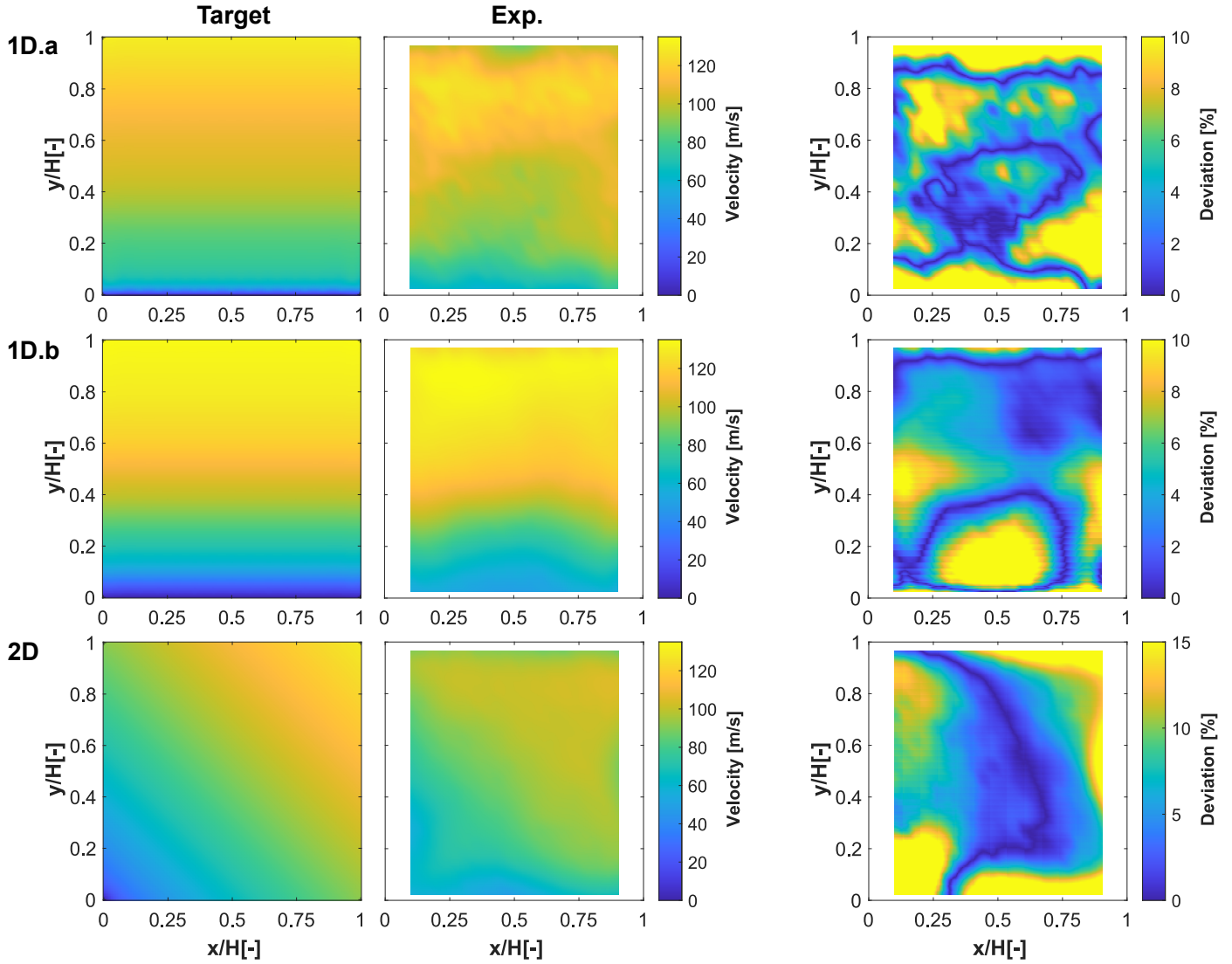
Figure 18: Experimental validation of the velocity contours, comparing the values from the experiments against the the target for each case.

is almost identical to the numerical simulation and the target, regardless of small regions in the top and bottom of the section. As previously mentioned, those regions will never be replicated with the proposed method due to the presence of the boundary layer.

Moreover, for the reference 1D.a geometry, two Kiel probes further downstream were used to assess the hypothesis of the distortion conservation as the flow progresses down the duct. These additional probes are located 4.8 and 6.3 hydraulic diameters from the distortion screen. In Fig. 17 the results from these downstream measurements are shown, demonstrating how the desired velocity distribution is well-kept across the test section of the wind tunnel.

Finally, the data from the measurements performed in the cross-section for each one of the cases is represented in Fig. 18. As a consequence of physical limitations, the zones closest to the lateral walls cannot be reached by the probe, as well as those very close to the top and bottom. In

general terms, it can be said that the distributions are very alike to the targets. For the 1D.a case, the deviation from the target in almost the whole section is in the order of 4%, presenting a slight asymmetry with larger deviation values in the bottom-right. The 1D.b distribution shows a region in the lower part around the center where the deviation increases, induced by the accelerated flow already seen in the profile of Fig. 16. The rest of the section presents values also in the order of 4%. The 2D distortion screen is able to replicate the diagonal pattern in a very satisfactory way, even considering challenging conditions such as null velocity in one corner and a peak velocity above 120 m/s in the opposite one, or values different than zero near the walls. Values of the deviation with respect to the target are slightly larger than in the 1D cases, although with values around 5%.

For a more detailed analysis of the deviation of the actual measurements with respect to the target, Fig. 19 shows probability distribution functions of the percentage difference
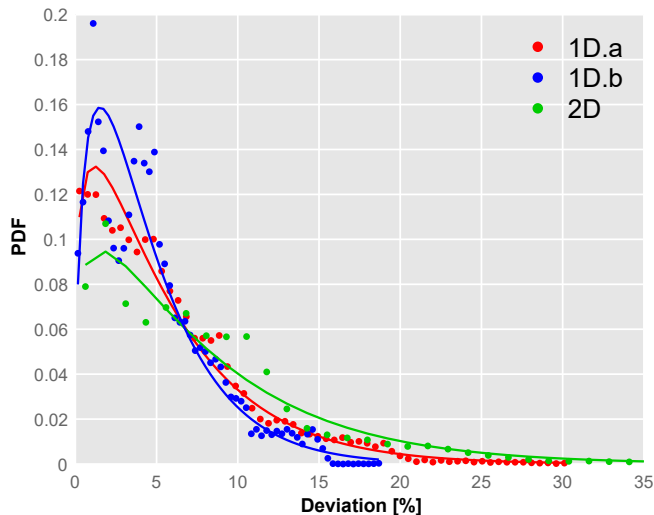
Figure 19: Probability Density Function of the deviation in the section comparing the target and the measured distribution for the three different cases. The continuous lines represent Γ distributions fits.

between the actual and desired velocity distributions. Dots represent the actual values whereas the curves are Γ fits for each distribution. It is shown how the 1D.a case presents the maximum earlier than any other, with a mean value of 5.72% and a skewness of 1.79. Although the 1D.b screen exhibits a region with large values of deviation, its maximum value is lower than any of the other distributions and, in fact, the average of its deviation is 4.57% and the skewness of the curve 1.63. In the 2D case, higher values of deviation are present, with a mean of 8.04% and a skewness of 1.8.

5. Summary and conclusions

In this article, a methodology to automatically generate distortion screens able to replicate a certain velocity distribution from a uniform velocity field has been presented. From a series of analytical models, the values of a porosity distribution that induces a controlled total pressure drop are derived and translated into geometrical positions of pores in the screen.

Three different cases, two 1D velocity variations and a bi-dimensional distribution, have been analysed numerically in the first place and experimentally afterwards. A $k - \omega$ SST RANS model has been used in the numerical analysis, predicting results with high similarity to the targets. In addition, it was seen that the induced velocity distribution was kept far downstream of the distortion panel and how it induced relatively large turbulence just after the zones with the closest pores, acting as flow straightener in the rest of the section. Furthermore, CFD results indicated that vorticity propagates downstream with large values close to the screen, justifying the need to leave a certain distance between the distortion panel and the measurement location.

Experimentally, it was confirmed that the actual distributions achieved in the wind tunnel match the target ones with deviations generally lower than 8% for most of the measured section, even for quite restrictive conditions. Additionally, the conservation of the velocity profile several hydraulic diameters downstream of the distortion screen has also been proved.

The model presents its major limitation when introducing non-physical velocity features (e.g. non-zero velocity too close to the walls) or sudden changes in the speed over short distances. Additionally, the fact that the theoretical model assumes a constant and uniform incoming velocity, turns into deviations in the actual measurements as the incoming flow may present irregularities and a boundary layer near the walls. Therefore, a future version could include a loop where the experimental measurements are used to further refine the automatised design.

In summary, it can be concluded that the proposed methodology is able to automatically generate a geometry that can be easily manufactured through AM and can replicate a target velocity distribution with good accuracy in a first attempt. This will assist in reducing expensive preparation times for aerodynamic tests in wind tunnels in which this kind of flow distortion is required, such as turbomachinery, engine inlets, internal aerodynamics, civil engineering and architecture studies among others.

Conflict of interest statement

The authors declare that they have no known competing financial interests or personal relationships that could have appeared to influence the work reported in this paper.

Acknowledgements

References

Ameur, K., Masson, C., Eecen, P.J., 2011. 2d and 3d numerical simulation of the wind-rotor/nacelle interaction in an atmospheric boundary layer. Journal of Wind Engineering and Industrial Aerodynamics 99, 833–844. doi:doi:10.1016/j.jweia.2011.06.002.

Andreassi, L., Cordiner, S., Mulone, V., 2004. Cell shape influence on mass transfer and backpressure losses in an automotive catalytic converter, in: 2004 SAE Fuels & Lubricants Meeting & Exhibition, pp. 2004–01–1837. doi:doi:10.4271/2004-01-1837.

Barlow, J.B., Rae, W.H., Pope, A., Pope, A., 1999. Low-speed wind tunnel testing. 3rd ed ed., Wiley.

Biswas, S., Kumar, J., Ganeshachar, M., Babu, S.N., Ramachandra, S., 2013. Fatigue failure of a distortion screen during testing. Procedia Engineering 55, 487–492. doi:doi:10.1016/j.proeng.2013.03.285.

Catarelli, R.A., Fernández-Cabán, P.L., Masters, F.J., Bridge, J.A., Gurley, K.R., Matyas, C.J., 2020. Automated terrain generation for precise atmospheric boundary layer simulation in the wind tunnel. Journal of Wind Engineering and Industrial Aerodynamics 207. doi:doi:10.1016/j.jweia.2020.104276.

Chavez Modena, M., González, L.M., Valero, E., Broatch, A., García-Tíscar, J., Felgueroso, A., 2021. Numerical and experimental analysis of thermo-aerodynamic performance in an aero engine surface heat exchanger, in: AIAA AVIATION 2021 FORUM, American Institute of Aeronautics and Astronautics. p. 15. doi:doi:10.2514/6.2021-2901.

Ecker, W.T., Mort, K.W., Jope, J., 1976. Aerodynamic design guidelines and computer program for estimation of subsonic wind tunnel performance. National Aeronautics and Space Administration.

Frohnapfel, D.J., Todd Lowe, K., O'Brien, W.F., 2020. Experimental quantification of fan rotor effects on inlet swirl using swirl distortion descriptors. Journal of Engineering for Gas Turbines and Power 140, 082603. doi:doi:10.1115/1.4039425.

Gelain, M.C., Couilleaux, A., Errera, M., Vicquelin, R., Gicquel, O., 2021. Conjugate heat transfer analysis of a surface air-cooled oil cooler (SACOC) installed in a turbofan by-pass duct., in: AIAA AVIATION 2021 FORUM, American Institute of Aeronautics and Astronautics. p. 22. doi:doi:10.2514/6.2021-3163.

Gibson, I., Rosen, D.W., Stucker, B., et al., 2014. Additive manufacturing technologies. volume 17. Springer.

Gorton, S., Owens, L., Jenkins, L., Allan, B., Schuster, E., 2004. Active flow control on a boundary-layer-ingesting inlet, in: 42nd AIAA Aerospace Sciences Meeting and Exhibit, American Institute of Aeronautics and Astronautics. p. 12. doi:doi:10.2514/6.2004-1203.

Guimarães, T., Lowe, K.T., O'Brien, W.F., 2019. Vortical flow development in round ducts across scales for engine inlet applications. Experiments in Fluids 60, 52. doi:doi:10.1007/s00348-019-2702-9.

Hart, K., 2008. Basic architecture and sizing of commercial aircraft gas turbine oil feed systems, in: Volume 4: Heat Transfer, Parts A and B, ASMEDC. pp. 1431–1441. doi:doi:10.1115/GT2008-50450.

Hong, S.W., Lee, I.B., Seo, I.H., 2015. Modelling and predicting wind velocity patterns for windbreak fence design. Journal of Wind Engineering and Industrial Aerodynamics 142, 53–64. doi:doi:10.1016/j.jweia.2015.03.007.

Huang, Y., He, X., Jiang, P., Zhu, H., 2020. Effect of non-uniform inlet velocity profile on flow field characteristics of a bluff body. Experimental Thermal and Fluid Science 118. doi:doi:10.1016/j.expthermflusci.2020.110152.

Koo, J.K., James, D.F., 1973. Fluid flow around and through a screen. Journal of Fluid Mechanics 60, 513. doi:doi:10.1017/S0022112073000327.

Kozmar, H., 2021. Flow, turbulence and surface pressure on a wall-mounted cube in turbulent boundary layers. Journal of Wind Engineering and Industrial Aerodynamics 210. doi:doi:10.1016/j.jweia.2020.104503.

Kulkarni, V., Sahoo, N., Chavan, S.D., 2011. Simulation of honeycomb-screen combinations for turbulence management in a subsonic wind tunnel. Journal of Wind Engineering and Industrial Aerodynamics 99, 37–45. doi:doi:10.1016/j.jweia.2010.10.006.

Lin, P., Wang, M., Wang, C., Fu, J., 2019. Abrupt stall detection for axial compressors with non-uniform inflow via deterministic learning. Neurocomputing 338, 163–171. doi:doi:10.1016/j.neucom.2019.02.007.

Lucas, J.R., O'Brien, W.F., Ferrar, A.M., 2014. Effect of BLI–type inlet distortion on turbofan engine performance, in: Volume 1A: Aircraft Engine; Fans and Blowers, American Society of Mechanical Engineers. p. V01AT01A037. doi:doi:10.1115/GT2014-26666.

McLelland, G., MacManus, D.G., Zachos, P.K., Gil-Prieto, D., Migliorini, M., 2020. Influence of upstream total pressure profiles on s-duct intake flow distortion. Journal of Propulsion and Power 36, 346–356. doi:doi:10.2514/1.B37554.

Menter, F., 1993. Zonal two equation k-w turbulence models for aerodynamic flows, in: 24th Fluid Dynamics Conference, American Institute of Aeronautics and Astronautics. p. 22. doi:doi:10.2514/6.1993-2906, arXiv:https://arc.aiaa.org/doi/pdf/10.2514/6.1993-2906.

Menter, F.R., Smirnov, P.E., Liu, T., Avancha, R., 2015. A one-equation local correlation-based transition model. Flow, Turbulence and Combustion 95, 583–619. doi:doi:10.1007/s10494-015-9622-4.

Migliorini, M., Zachos, P., MacManus, D., 2019. The impact of inlet boundary layer thickness on the unsteady aerodynamics of s-duct intakes, in: AIAA Propulsion and Energy 2019 Forum, American Institute of Aeronautics and Astronautics. p. 15. doi:doi:10.2514/6.2019-4202.

Mirkov, N., Rašuo, B., Kenjereš, S., 2015. On the improved finite volume procedure for simulation of turbulent flows over real complex terrains. Journal of Computational Physics 287, 18–45. doi:doi:10.1016/j.jcp.2015.02.001.

Ocokoljić, G., Damljanović, D., Vuković, D., Rašuo, B., 2018. Contemporary frame of measurement and assessment of wind-tunnel flow quality in a low-speed facility. FME Transactions 46, 429–442. doi:doi:10.5937/fmet1804429O.

Overall, B., 1972. A procedure for the design of complex distortion screen patterns for producing specified steady-state total pressure profiles at the inlet of turbine engines, in: Report AD890870, US Air Force, p. 56.

Owen, P.R., Zienkiewicz, H.K., 1957. The production of uniform shear flow in a wind tunnel. Journal of Fluid Mechanics 2, 521. doi:doi:10.1017/S0022112057000336.

O'Neill, F., 2006. Source models of flow through and around screens and gauzes. Ocean Engineering 33, 1884–1895. doi:doi:10.1016/j.oceaneng.2005.10.009.

Paduano, J., Greitzer, E., Epstein, A., 2001. Compression system stability and active control. Annual Review of Fluid Mechanics 33, 491–517. doi:doi:10.1146/annurev.fluid.33.1.491.

Paniagua, G., Cuadrado, D., Saavedra, J., Andreoli, V., Meyer, T., Solano, J.P., Herrero, R., Meyer, S., Lawrence, D., 2018. Design of the Purdue Experimental Turbine Aerothermal Laboratory for Optical and Surface Aerothermal Measurements. Journal of Engineering for Gas Turbines and Power 141. doi:doi:10.1115/1.4040683.

Phillips, J.C., Thomas, N.H., Perkins, R.J., Miller, P.C.H., 1999. Wind tunnel velocity profiles generated by differentially-spaced flat plates. Journal of Wind Engineering and Industrial Aerodynamics 80, 253–262. doi:doi:10.1016/S0167-6105(98)00207-4.

Provenza, A.J., Duffy, K.P., Bakhle, M.A., 2019. Aeromechanical response of a distortion-tolerant boundary layer ingesting fan. Journal of Engineering for Gas Turbines and Power 141, 011011. doi:doi:10.1115/1.4040739.

Rasuo, B., 2011. The influence of reynolds and mach numbers on two-dimensional wind-tunnel testing: An experience. Aeronautical Journal 115, 249–254. doi:doi:10.1017/S0001924000005704.

Rasuo, B., 2012. Scaling between wind tunnels-results accuracy in two-dimensional testing. Transactions of the Japan Society for Aeronautical & Space Sciences 55, 109–115.

Roach, P., 1987. The generation of nearly isotropic turbulence by means of grids. International Journal of Heat and Fluid Flow 8, 82–92. doi:doi:10.1016/0142-727X(87)90001-4.

S-16 Turbine Engine Inlet Flow Distortion Committee, 2017. A methodology for assessing inlet swirl distortion, in: A Methodology for Assessing Inlet Swirl Distortion, p. 110. doi:doi:10.4271/AIR5686.

Saini, D., Shafei, B., 2021. High-fidelity prediction of flight trajectories of plate-type debris in boundary layer winds. Journal of Wind Engineering and Industrial Aerodynamics 217. doi:doi:10.1016/j.jweia.2021.104727.

Saleem Yusoof, M., Sivapragasam, M., Deshpande, M., 2016. Strip distortion generator for simulating inlet flow distortion in gas turbine engine ground test facilities. Propulsion and Power Research 5, 287–301. doi:doi:10.1016/j.jppr.2016.11.004.

Salunkhe, P.B., Joseph, J., Pradeep, A.M., 2011. Active feedback control of stall in an axial flow fan under dynamic inflow distortion. Experimental Thermal and Fluid Science 35, 1135–1142. doi:doi:10.1016/j.expthermflusci.2011.03.008.

Schneck, W., Ferrar, A., Bailey, J., Hoopes, K., O'Brien, W., 2013. Improved prediction method for the design of high-resolution total pressure distortion screens, in: 51st AIAA Aerospace Sciences Meeting including the New Horizons Forum and Aerospace Exposition, American Institute of Aeronautics and Astronautics. p. 19. doi:doi:10.2514/6.2013-1133.

Sivapragasam, M., 2019. Flow field behind a complex total pressure distortion screen. Proceedings of the Institution of Mechanical Engineers, Part G: Journal of Aerospace Engineering 233, 5075–5092. doi:doi:10.1177/0954410019837862.

Steiros, K., Hultmark, M., 2018. Drag on flat plates of arbitrary porosity. Journal of Fluid Mechanics 853, 11. doi:doi:10.1017/jfm.2018.621.

Stephens, J.E., Celestina, M., Hughes, C., 2019. Swirl distortion using stream vanes for boundary layer ingestion research, in: Volume 2A: Turbomachinery, American Society of Mechanical Engineers. p. V02AT39A035. doi:doi:10.1115/GT2019-92073.

Stojaković, P., Rasuo, B., 2016a. Minimal safe speed of the asymmetrically loaded combat airplane. Aircraft Engineering and Aerospace Technology 88, 42–52. doi:doi:10.1108/AEAT-03-2014-0033.

Stojaković, P., Rasuo, B., 2016b. Single propeller airplane minimal flight speed based upon the lateral maneuver condition. Aerospace Science and Technology 49, 239–249. doi:doi:10.1016/j.ast.2015.12.012.

Stojaković, P., Velimirović, K., Rašuo, B., 2018. Power optimization of

a single propeller airplane take-off run on the basis of lateral maneuver limitations. Aerospace Science and Technology 72, 553–563. doi:doi:10.1016/j.ast.2017.10.015.

Tan, C., Day, I., Morris, S., Wadia, A., 2010. Spike-type compressor stall inception, detection, and control. Annual Review of Fluid Mechanics 42, 275–300. doi:doi:10.1146/annurev-fluid-121108-145603.

Tanguy, G., MacManus, D.G., Garnier, E., Martin, P.G., 2018. Characteristics of unsteady total pressure distortion for a complex aeroengine intake duct. Aerospace Science and Technology 78, 297–311. doi:doi:10.1016/j.ast.2018.04.031.

Taylor, J.V., 2019. Complete flow conditioning gauzes. Experiments in Fluids 60, 35. doi:doi:10.1007/s00348-019-2682-9.

Toge, T.D., Pradeep, A., 2017. Experimental investigation of stall inception of a low speed contra rotating axial flow fan under circumferential distorted flow condition. Aerospace Science and Technology 70, 534–548. doi:doi:10.1016/j.ast.2017.08.041.

Tse, K.T., Weerasuriya, A.U., Kwok, K.C., 2016. Simulation of twisted wind flows in a boundary layer wind tunnel for pedestrian-level wind tunnel tests. Journal of Wind Engineering and Industrial Aerodynamics 159, 99–109. doi:doi:10.1016/j.jweia.2016.10.010.

Valencia, E., Alulema, V., Rodriguez, D., Laskaridis, P., Roumeliotis, I., 2020. Novel fan configuration for distributed propulsion systems with boundary layer ingestion on an hybrid wing body airframe. Thermal Science and Engineering Progress 18, 100515. doi:doi:10.1016/j.tsep.2020.100515.

Walsh, P.P., Fletcher, P., 2004. Gas turbine performance. 2nd ed ed., Blackwell Science. doi:doi:10.1002/9780470774533.

Zenger, F.J., Renz, A., Becher, M., Becker, S., 2016. Experimental investigation of the noise emission of axial fans under distorted inflow conditions. Journal of Sound and Vibration 383, 124–145. doi:doi:10.1016/j.jsv.2016.07.035.